energies

MDPI

Article

Reversible Molten Catalytic Methane Cracking Applied to Commercial Solar-Thermal Receivers

Scott C. Rowe [1], Taylor A. Ariko [2], Kaylin M. Weiler [2], Jacob T. E. Spana [2] and Alan W. Weimer [1,*]

[1] Chemical & Biochemical Engineering, University of Colorado Boulder, Boulder, CO 80309, USA; scott.rowe@colorado.edu

[2] Chemical Engineering, Florida State University, Tallahasse, FL 32306, USA; taa15b@my.fsu.edu (T.A.A.); kw17e@my.fsu.edu (K.M.W.); jts15b@my.fsu.edu (J.T.E.S.)

* Correspondence: alan.weimer@colorado.edu

Received: 24 October 2020; Accepted: 23 November 2020; Published: 26 November 2020

check for updates

Abstract: When driven by sunlight, molten catalytic methane cracking can produce clean hydrogen fuel from natural gas without greenhouse emissions. To design solar methane crackers, a canonical plug flow reactor model was developed that spanned industrially relevant temperatures and pressures (1150–1350 Kelvin and 2–200 atmospheres). This model was then validated against published methane cracking data and used to screen power tower and beam-down reactor designs based on "Solar Two," a renewables technology demonstrator from the 1990s. Overall, catalytic molten methane cracking is likely feasible in commercial beam-down solar reactors, but not power towers. The best beam-down reactor design was 9% efficient in the capture of sunlight as fungible hydrogen fuel, which approaches photovoltaic efficiencies. Conversely, the best discovered tower methane cracker was only 1.7% efficient. Thus, a beam-down reactor is likely tractable for solar methane cracking, whereas power tower configurations appear infeasible. However, the best simulated commercial reactors were heat transfer limited, not reaction limited. Efficiencies could be higher if heat bottlenecks are removed from solar methane cracker designs. This work sets benchmark conditions and performance for future solar reactor improvement via design innovation and multiphysics simulation.

Keywords: solar-thermal; methane cracking; concentrated solar

1. Introduction

Unlike prior hydrocarbons-to-hydrogen chemistries that produce greenhouse gases [1,2], catalytic methane cracking makes solid carbon for sequestration or reuse [3]. When driven with solar heat, this reaction can generate greenhouse-neutral hydrogen fuel from carbonaceous feedstocks, a transitional technology towards fully sustainable infrastructure [4–13]. Figure 1 shows the concept, wherein a macroscopic reactor harbors microscopic reaction. Within this regime methane bubbles through a melt of liquid bismuth and catalytic nickel:

$$CH_4(g) \underset{27\%Ni(l),\ 73\%Bi(l)}{\rightleftarrows} 2H_2(g) + C(s)$$

As the bubbles rise heat drives endothermic methane conversion to hydrogen gas and graphitic carbon, a chemistry pioneered within an indirectly heated tubular bubbler [3]. Commercial solar-thermal technologies, exemplified by the Solar Two pilot plant [14], similarly heat fluids indirectly within tubes, tubes that intercept concentrated sunlight from heliostats. However, current solar thermal facilities operate at 500 °C [15], whereas molten catalytic methane cracking occurs at higher temperatures (>1000 °C). Higher temperatures can only magnify the radiative and convective heat losses observed in a Solar Two design [15,16]. Thus, although the "Solar Two" approach is mature, its feasibility for molten catalytic methane cracking is unclear.

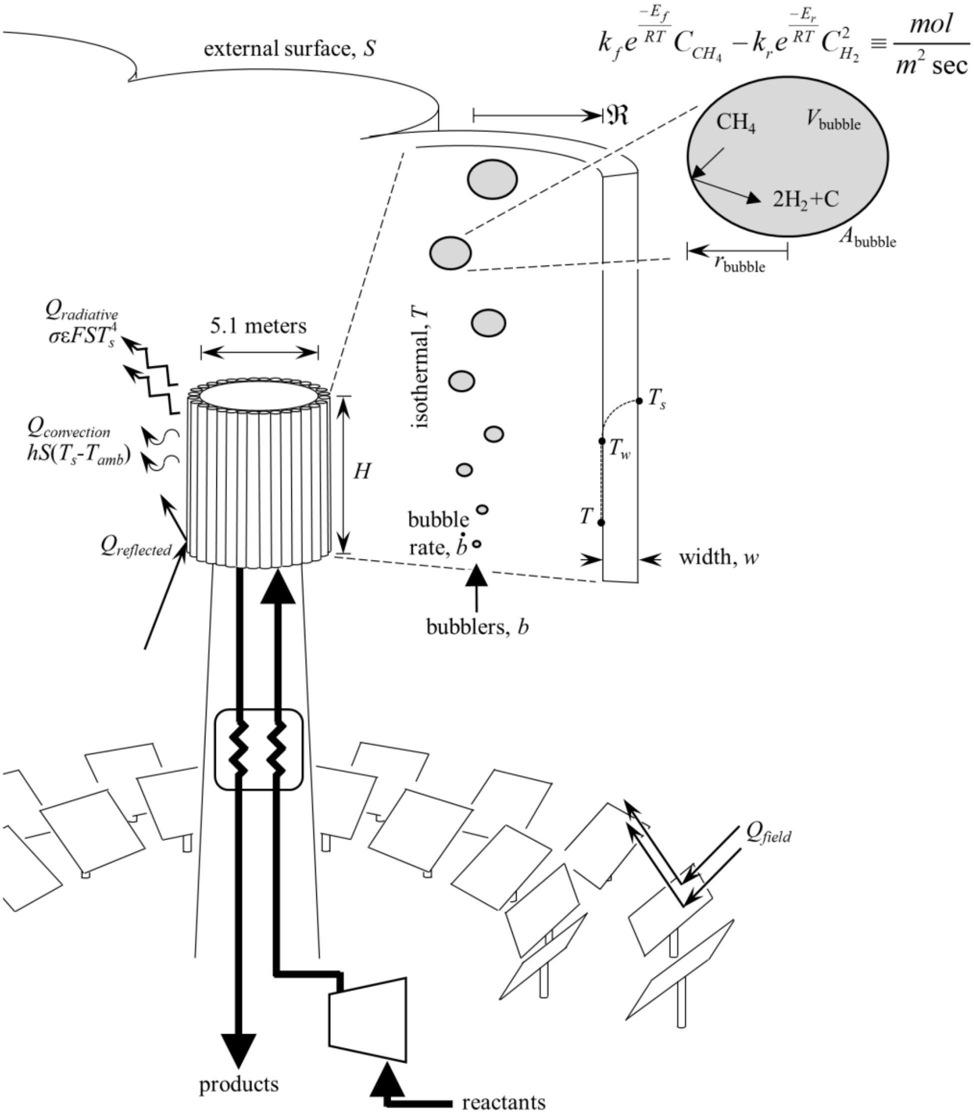

Figure 1. Multiscale characteristics of solar catalytic molten methane cracking in a "Solar Two" configuration [14].

Recently, an alternative to Solar Two power tower designs premiered at commercial scale [17]. Figure 2 compares Solar Two to the new configuration, which places the tubular receiver at or below the heliostat field. This beam-down receiver is exposed to the environment only through an open aperture that accepts light from a suspended reflector. Compared to a fully exposed Solar Two power tower, this nested receiver can reduce convective and emissive heat losses. However, new losses are associated with light reflection and redirection into the beam-down aperture [17]. Potential solar performance improvements with a beam-down, versus established power tower design, is explored herein.

Tractable solar driven methane cracking with a power tower or beam-down design likely lies within the large range of reaction temperatures and pressures common in industrial practice, which can reach 1100° Celsius and 400 atmospheres [18]. Over these extreme conditions reaction may be reversible, a facet omitted from recent studies of catalytic methane cracking [3,19–22]. Catalytic molten methane kinetics were revisited to evaluate reactor performance over these expansive conditions and explore likely reaction reversibility in industrial implementations.

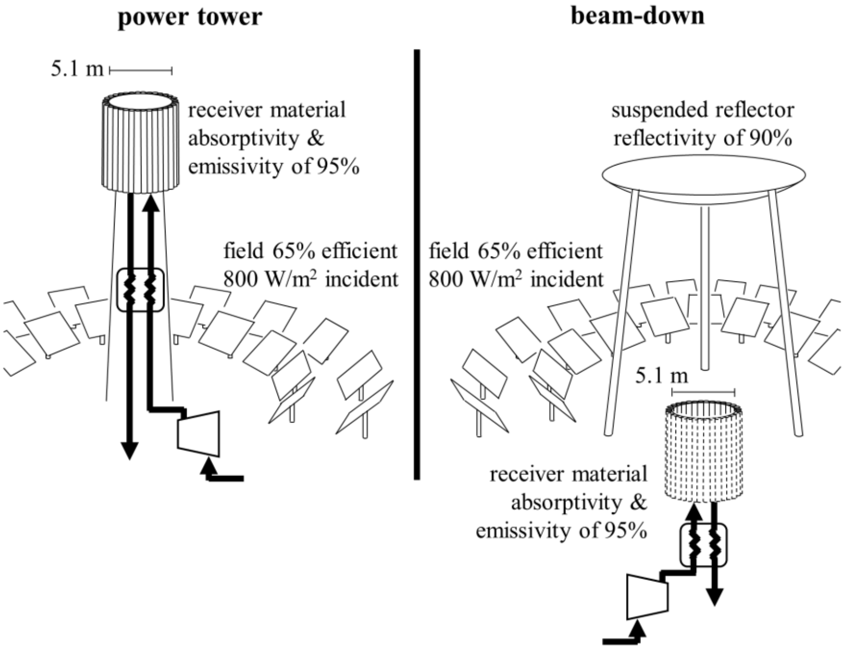

Figure 2. Characteristics of solar catalytic molten methane cracking in a "Solar Two" [14] configuration or an analogous beam-down configuration.

2. Materials and Methods

2.1. Reversible Catalytic Molten Methane Cracking Kinetics

In prior reactor design and economics, authors have assumed that methane cracking is irreversible [3,19–22]. However, heterogeneous and noncatalytic methane decomposition is reversible and inhibited by high pressure [23–30], an effect that can cause the thermodynamic limitation of hydrogen production [31]. Thus, to evaluate the performance of a multitube solar receiver across industrially relevant conditions, catalytic methane cracking kinetics were expanded to feature reaction reversion at extreme temperatures and pressures. Specifically, a kinetics model was proposed based on the batch surface catalyzed decomposition of methane in a spherical isothermal bubble [3,32]:

$$\frac{dn_{CH_4}}{dt} = -A_{bubble}rate \tag{1}$$

$$\frac{dn_C}{dt} = A_{bubble}rate \tag{2}$$

$$\frac{dn_{H_2}}{dt} = 2A_{bubble}rate \tag{3}$$

$$A_{bubble} = 4\pi r_{bubble}^2 \tag{4}$$

A table of variable definitions is available in Appendix A. Here, A_{bubble} is the bubble surface area based on bubble radius r_{bubble}. Changes in carbon n_C, methane n_{CH4}, and hydrogen n_{H2} moles depend on the reaction rate, which conformed to literature-established Arrhenius expressions for reversible methane decomposition [23–30]:

$$rate = k_f e^{\frac{-E_f}{RT}} C_{CH_4} - k_r e^{\frac{-E_r}{RT}} C_{H_2}^2 \tag{5}$$

The expansion of bubble surface and size is strongly influenced by pressure, which varies with elevation within a dense molten metal [33,34]:

$$P(z) = P_{inlet} - \rho g z \tag{6}$$

Specifically, positional pressure $P(z)$ depends on the reactor inlet pressure P_{inlet}, the temperature-dependent liquid metal density ρ, the acceleration of gravity g, and elevation z within a reactor tube. Appendix B lists property correlations, including the expression for liquid metal catalyst density ρ. Like pressure, volumetric flow through a reactor is similarly elevation dependent, but dictated by reactor material conservation at steady state:

$$\dot{Q}(z) = \frac{[\dot{n}_{CH_4}(z) + \dot{n}_{H_2}(z)]ZRT}{P(z)} = \frac{\dot{n}(z)}{\rho(z)} \tag{7}$$

Here, solid carbon contributes negligible volumetric flow, but the volumetric flows of gaseous methane $\dot{n}_{CH4}$ and hydrogen $\dot{n}_{H2}$ are assumed substantial. Thus, the positional volumetric flow is a function of isothermal reaction temperature T, pressure $P(z)$, and gas mole flows. Compressibility Z was calculated via the SRK equation of state with Kay's rule [35]. Effective bubble area can be modeled from volumetric flow at a given elevation if the rate of bubble emanation $\dot{b}$ (bubbles/second) is known:

$$\dot{Q}(z) = \dot{b}V_{bubble} = \dot{b}\frac{4\pi r_{bubble}^3}{3}, \qquad r_{bubble} = \left(\frac{A_{bubble}(z)}{4\pi}\right)^{1/2} \tag{8}$$

Combining these two equations gives the approximate elevation-dependent bubble catalytic surface in a molten metal:

$$A_{bubble}(z) = \left(\frac{6\pi^{1/2}\dot{Q}(z)}{\dot{b}}\right)^{2/3} \tag{9}$$

This equation assumes insubstantial bubble coalescence, a phenomena that would alter bubble area A_{bubble}. Sieve plates and/or impellers can disaggregate and avert bubble coalescence, as is common in extractive distillation [36–38].

These equations combine to yield a differential-algebraic system for analyzing a single isothermal molten catalytic methane bubbler:

$$P(z) = P_{inlet} - \rho g z \tag{10}$$

$$\dot{Q}(z) = \frac{[\dot{n}_{CH_4}(z) + \dot{n}_{H_2}(z)]ZRT}{P(z)} \tag{11}$$

$$A_{bubble}(z) = \left(\frac{6\pi^{1/2}\dot{Q}(z)}{\dot{b}}\right)^{2/3} \tag{12}$$

$$y_{CH_4} = \frac{\dot{n}_{CH_4}(z)}{\dot{n}_{CH_4}(z) + \dot{n}_{H_2}(z)} \tag{13}$$

$$y_{H_2} = \frac{\dot{n}_{H_2}(z)}{\dot{n}_{CH_4}(z) + \dot{n}_{H_2}(z)} \tag{14}$$

$$C_{CH_4} = y_{CH_4}\frac{P(z)}{ZRT} \tag{15}$$

$$C_{H_2} = y_{H_2}\frac{P(z)}{ZRT} \tag{16}$$

$$rate = k_f e^{\frac{-E_f}{RT}} C_{CH_4} - k_r e^{\frac{-E_r}{RT}} C_{H_2}^2 \tag{17}$$

$$\frac{d\dot{n}_{CH_4}}{dz} = -bA_{bubble}rate \tag{18}$$

$$\frac{d\dot{n}_C}{dz} = bA_{bubble}rate \tag{19}$$

$$\frac{d\dot{n}_{H_2}}{dz} = 2bA_{bubble}rate \tag{20}$$

where y is mole fraction and C is the concentration of the respective subscripted species. Notably, a tubular reactor could contain multiple bubblers ($b > 1$). The rate of bubble emanation is then dependent on the feed flowrate $\dot{n}_{inlet}$ and bubble inlet orifice radius $r_{bubble,inlet}$:

$$\dot{b} = \frac{\dot{n}_{inlet}}{\rho_{inlet}V_{bubble,inlet}} = \frac{\dot{n}_{inlet}}{(P_{inlet}/(ZRT))(4\pi r^3_{bubble,inlet}/3)} \tag{21}$$

The feed flowrate is determined by the velocity of bubbles at the inlet temperature and pressure, which was calculated via the work of Davies and Taylor (1950) [39]:

$$\dot{n}_{inlet} = \rho_{gas}\dot{V} = \frac{P_{inlet}}{ZRT}(A_{bubblers}v_{bubbler}) = \frac{P_{inlet}}{ZRT}\left(A_{bubblers}\frac{2}{3}\sqrt{gr_{bubble,inlet}}\right) \tag{22}$$

$A_{bubblers}$ refers to the active bubbling area of a reactor gas distributor, which was 25% of the reactor floor, as is common in distillation [36]. Thus, the number of bubblers in a tubular reactor was:

$$A_{bubblers} = 0.25A_{tube}, \quad b = \frac{A_{bubblers}}{\pi r^2_{bubble,inlet}} \tag{23}$$

where A_{tube} is the tubular reactor cross-sectional area. An initial bubble size of $r_{bubble,inlet}$ = 0.5 cm was adopted, which conforms to the work of Upham et al. 2017 [3] and lumps bubble internal diffusion into the overall kinetic model.

2.2. Thermal Reactor Model

Exterior solar illumination must trespass multiple thermal barriers to heat reacting methane (Figure 1), barriers that limit solar energy ingress [15]. Such indirect solar heating is known to be limiting in solar reactor and thermal systems [40,41]. Conversely, bubbling molten metals rapidly transport thermal energy through strong convection and conduction (Metals, 1954). Thus, temperature was considered isothermal in the liquid metal catalyst, but likely barriers to solar heat were modeled in the reactor geometry presented in Figure 1. Specifically, Solar Two was a ø5.1 m circular receiver lined with Inconel tubes and we adopt the same configuration here [14], but vary reaction tube radius from 1 cm to the maximal extrusions considered feasible in Inconel piping manufacture (0.5 m) [42]. In the beam-down configuration, tubes were heated from cavity internal surfaces, versus externally in the original Solar Two power tower design. Losses through natural convection to ambient air around the receiver exterior surface S were modeled as previously described for concentrated solar facilities [43]:

$$Q_{convection} = hS(T_s - T_{amb}) \tag{24}$$

where h was calculated as shown in Boehm et al. 1987 for natural convection from a power tower or cavity receiver (Appendix B). The heated receiver surface S in m^2 was simulated at temperature T_s relative to an ambient condition of T_{amb} = 298.15 Kelvin. Energy transfer between reactor tubular walls and molten metal was similarly driven by a heat transfer coefficient h_{wall}, but for a constant Nusselt number of 4.8 typical of liquid metals [44] (Appendix B):

$$Q_{wall} = h_{wall}S(T_{wall} - T) \tag{25}$$

where T is the isothermal reaction temperature (Figure 1). The overall heated reactor surface S is dictated by the number of tubular reactors n in a receiver manifold, the arc each tube presented to the environment ϕ, the tube height H, and the outer tube radius $\mathfrak{R}$ + w:

$$S = n\phi H(\mathfrak{R} + w) \tag{26}$$

The tube radius was assessed from 0.01 to 0.5 m in all reactor designs, where extruded tubes larger than Ø1 m were considered infeasible [42]. Bubbler Inconel wall thickness and wall temperature profiles were found through simultaneous solution of the hoop stress formula and Fourier's law [45,46] (Appendix B):

$$\int_{\mathfrak{R}}^{\mathfrak{R}+w} N(r)dr = -\int_{T_w}^{T_s} k(T)dT \tag{27}$$

$$\sigma_{YS}(T_s)w = (\mathfrak{R} + w) * P_{inlet} \tag{28}$$

where the Inconel temperature dependent thermal conductivity, yield stress $\sigma_{YS}(T_s)$, and heat flux $N(r)$ were evaluated at their radial or extremum values.

Heliostats that direct light onto a receiver can be only 65% efficient [47–49]. Thus, only 65% of 800 W/m^2 sunlight incident on a heliostat field reached the reactor. The effective absorptivity and emissivity of corrugated receiver surfaces were determined by 2D Monte Carlo ray tracing in CUtrace [50], an opensource ray tracer, for uniformly radial incoming receiver irradiance, diffuse reflection, and diffuse emission (Appendix B). In traces, native reactor Inconel reflectivity was 5%, emissivity was 95%, and absorptivity was 95%, values that conform to prior experimental work with nickel alloy tubes [51]. Diffuse reflection and radiative emission from the beam-down reactor cavity were calculated via analytical view factors [16] (Appendix B), where ultimate emissive losses from a receiver were given by the Stefan–Boltzmann Law:

$$Q_{radiative} = \varepsilon\sigma FST_s^4 \tag{29}$$

where ε is the effective surface emissivity from ray tracing, σ the Stefan–Boltzmann constant, and F is the view factor if relevant (Appendix B).

For power tower designs necessary irradiance onto the heliostat field (facility power Q_{field}) was found from the overall energy balance given radiative losses, convective losses, and energy sunk into endothermic methane cracking:

$$0.65\alpha \underbrace{Q_{field}}_{\substack{\text{solar energy}\\ \text{intercepted by}\\ \text{the heliostat}\\ \text{field}}} = \underbrace{n\Delta H_{rxn}\dot{n}_{inlet}X}_{\textit{energy consumed by reaction}} + \underbrace{Q_{convection}}_{\textit{energy lost to air convection}} + \underbrace{Q_{radiative}}_{\textit{energy lost to reradiation}} \tag{30}$$

where the effective receiver absorptivity α was found from 2D Monte Carlo ray tracing. The 0.65 multiplicand originated from heliostat field efficiency [47–49]. For beam-down designs, this field efficiency was 10% lower to account for the redirection of light from a suspended reflector [52,53]:

$$0.585\alpha \underbrace{Q_{field}}_{\substack{\text{solar energy}\\ \text{intercepted by}\\ \text{the heliostat}\\ \text{field}}} = \underbrace{n\Delta H_{rxn}\dot{n}_{inlet}X}_{\textit{energy consumed by reaction}} + \underbrace{Q_{convection}}_{\textit{energy lost to air convection}} + \underbrace{Q_{radiative}}_{\textit{energy lost to reradiation}} \tag{31}$$

Additionally, reactor absorptivity was modified by view factors for diffuse reflection from the beam-down cavity. Reactor efficiency, the fractional energy sunk into hydrogen production versus overall sunlight collected, is:

$$\eta = \frac{n\Delta H_{rxn}\dot{n}_{inlet}X}{Q_{field}} = \frac{\text{energy into reaction}}{\text{solar energy into facility}} \tag{32}$$

3. Results

3.1. Validation of Reversible Catalytic Molten Methane Cracking Kinetics

To validate the proposed kinetics, especially the use of reactor material conservation for catalytic area calculation, Equation (5) Arrhenius coefficients k_1, k_2, E_f, and E_r were fit to data from Upham et al. 2017 [3]. This isothermal molten methane bubbler, filled with 27% nickel and 73% bismuth, operated at low pressure (200 kPa) and high temperature (1040 °C) where forward reaction dominates. Thus, nonlinear regression was initialized with the activation energy and Arrhenius preexponential of Upham et al. 2017 (E_f = 208 kJ/mol, k_f = 78,813 m/sec). However, that work provided no Arrhenius k_r and E_r for reversible kinetics. Thus, a preexponential and activation energy for reverse reaction were inferred from transition-state theory and van 't Hoff equation predictions [31,54] (Appendix B):

$$E_r \approx E_f - \Delta H_{rxn}(T) \tag{33}$$

$$\ln(K_c) \approx \ln\left(\frac{k_f e^{-E_f/RT}}{k_r e^{-E_r/RT}}\right) \approx \frac{-\Delta H_{rxn}(T)}{RT} \tag{34}$$

Subsequent nonlinear regression refined initial parameter estimates with equilibrium decomposition data from the literature [28,55,56]. Figures 3 and 4 show that discovered parameters for the new kinetics model predicted experimental data from Upham et al. 2017 and published methane equilibria [3,28,55,56]. Table 1 compares the discovered kinetic coefficients k_f, k_r, E_f, and E_r for catalytic methane cracking to prior work for noncatalytic reaction [29,30]. The discovered activation barrier for catalytic hydrogen production (k_f = 209 kJ/mol) was substantially lower than values from noncatalytic work (E_f = 284 kJ/mol and E_f = 337 kJ/mol) [29,30], consistent with catalysis. Disparate k_f and k_r preexponentials, which result from attempts to match methane decomposition equilibria, were evident in all reversible kinetic models (Table 1). Figure 4 shows that the new reversible kinetic model fit published methane decomposition equilibrium data K_c better than prior studies [28–30,55,56].

The reversible models in Table 1 differ from previous work that relied only on k_f and E_f [3,19–22]. These irreversible kinetic models set $k_r = 0$, which disallows the prediction of reaction equilibria. Thus, eliminating k_r likely yields an insufficient parameterization for accurate kinetics at extreme industrial reactor conditions [31]. Here, omitting k_r visibly and persistently inflated results at methane conversions larger than 60% (Figure 3). Thus, although there was substantial uncertainty in the reverse Arrhenius preexponential (k_r, Table 1), even at mild pressure (Figure 3, 200 kPa) the known reversibility of methane cracking had effects (Figure 3) [23–30].

The reversible catalytic methane kinetics discovered (Table 1, Equation (5)) have implications for reactor design. These reaction effects are summarized as a three-dimensional Levenspiel plot in Figure 5 [57]. Figure 5 shows that low pressure and high temperature enhance reaction rate and hydrogen production. However, dilute gas conditions at these conditions impede dense and productive reactor throughput. Conversely, high pressures support rate and allow dense reactor throughout, but limit maximal methane conversion via Le Chatelier's principle. Thus, high pressure constrains maximal reaction extent. Figure 5 overlays these and other tradeoffs that result from reaction equilibrium.

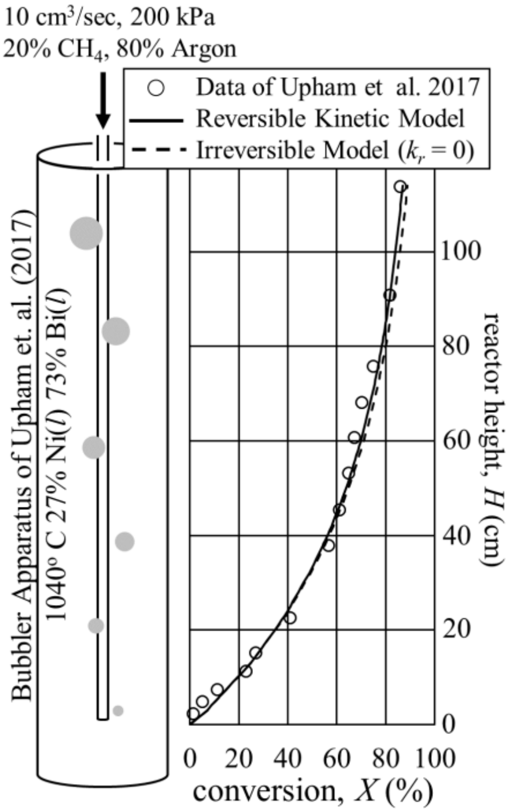

Figure 3. The application of reversible molten methane cracking kinetics to data from Upham et al. 2017 [3].

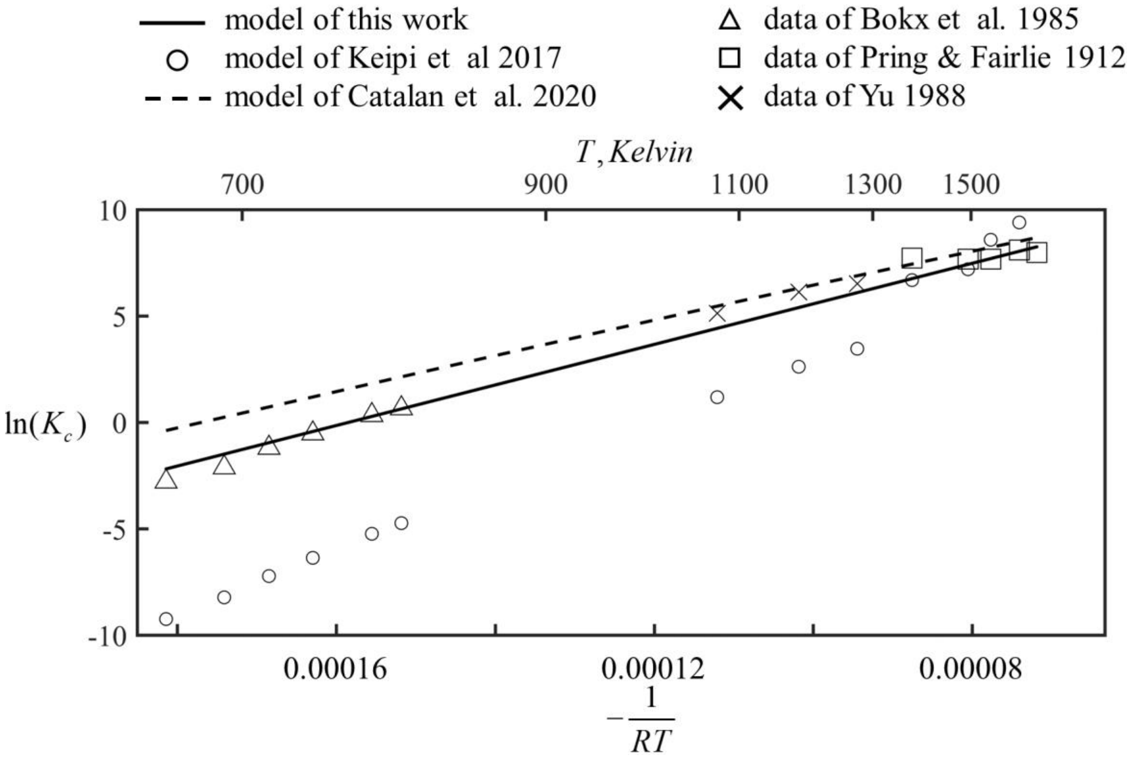

Figure 4. An Arrhenius plot of reaction equilibrium constant K_c predictions from reversible methane cracking kinetic models compared to published equilibrium data from experiments [28–30,55,56].

Table 1. Fitted kinetic parameters for reversible catalytic molten methane cracking with 95% confidence intervals compared to prior models of noncatalytic methane cracking [29,30]. Prior models from Keipi et al. 2017 and Catalan et al. 2020 were rearranged into identifiable forward and reverse Arrhenius expressions.

This work:				$rate\left[\frac{mol}{m^2\,\mathrm{sec}}\right] = k_f e^{\frac{-E_f}{RT}} C_{CH_4} - k_r e^{\frac{-E_r}{RT}} C_{H_2}^2$
k_f	221,765.4461	± 4,616	m/sec	
k_r	0.0613	± 0.0377	m^4/sec	
E_f	209.290	± 4.630	kJ/mol	$equilibrium\ K_c = \frac{C_{H_2}^2}{C_{CH_4}} = \frac{k_f e^{-E_f/RT}}{k_r e^{-E_r/RT}}$
E_r	114.028	± 4.630	kJ/mol	
Catalan et al. (2020)				$rate\left[\frac{mol}{m^3\,\mathrm{sec}}\right] = k_f e^{\frac{-E_f}{RT}} C_{CH_4}^n - k_r e^{\frac{-E_r}{RT}} C_{H_2}^2 C_{CH_4}^{n-1} T$
k_f	14,676.0000000		$m^{3n}mol/(mol^n m^3 sec)$	
k_r	0.0000021		$m^{3(2+m)}mol/(mol^m m^3 sec)$	
E_f	284.948		kJ/mol	
E_r	193.743		kJ/mol	$equilibrium\ K_c = \frac{C_{H_2}^2}{C_{CH_4}} = \frac{k_f e^{-E_f/RT}}{k_r e^{-E_r/RT} T}$
n	1.0809			
Keipi et al. (2017)				
k_f	8.5708*10^{12}		$cm^{3n}mol/(mol^n cm^3 sec)$	$rate\left[\frac{mol}{cm^3\,\mathrm{sec}}\right] = k_f e^{\frac{-E_f}{RT}} C_{CH_4}^n - k_r e^{\frac{-E_r}{RT}} C_{H_2}^m$
k_r	1.119*10^7		$cm^{3m}mol/(mol^m cm^3 sec)$	
E_f	337.120		kJ/mol	
E_r	243.160		kJ/mol	$equilibrium\ K_c = \frac{C_{H_2}^2}{C_{CH_4}} = \frac{k_f e^{-E_f/RT} C_{H_2}^{2-m}}{k_r e^{-E_r/RT} C_{CH_4}^{1-n}}$
n	1.1230			
m	0.9296			

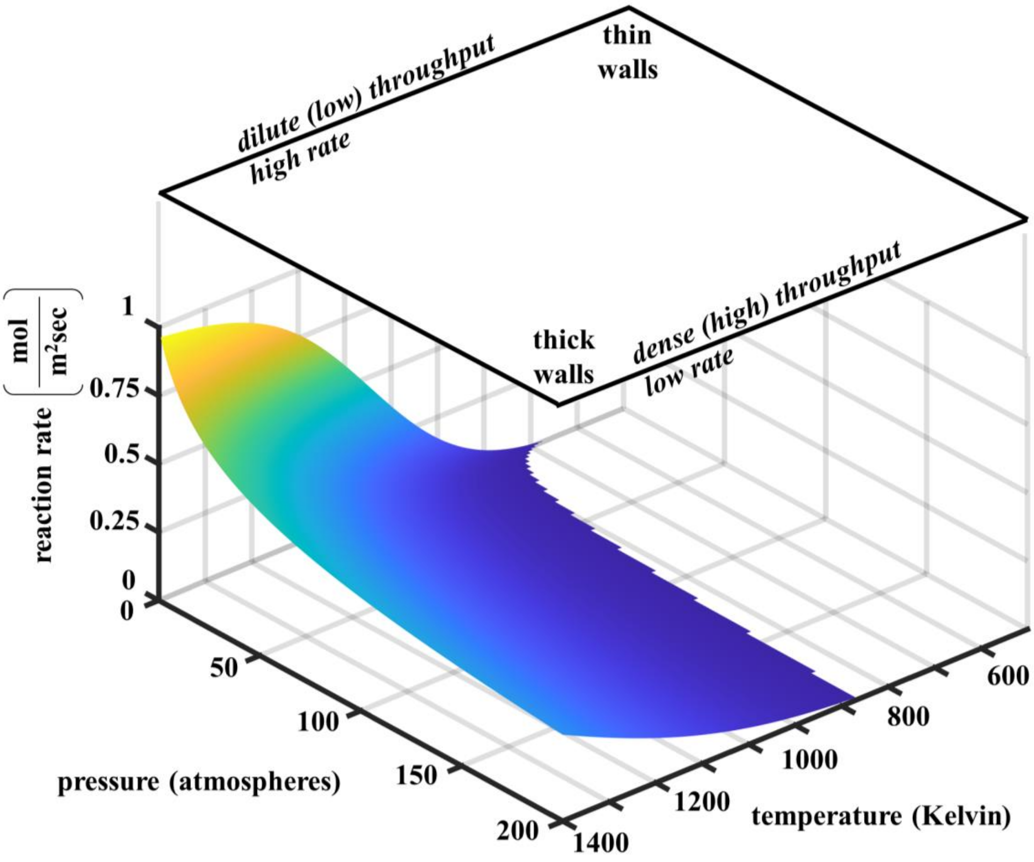

Figure 5. Reactor design implications given reversible catalytic molten methane cracking.

3.2. Solar Reactor Screening and Evaluation

Solar methane crackers were simulated for inlet reactant pressures from 2 to 200 atmospheres and isothermal reaction temperatures from 1150 to 1350 Kelvin, reasonable conditions in industrial practice [18,31]. Figure 6 shows simulation results after program execution on an 84 core computer. Where extreme conditions caused meltdown of the Inconel receiver, data is absent in this and subsequent figures. Solar receivers were evaluated for a pure methane feed and reactor tube radii from 0.01 to 0.5 m [42,58]. A reactor (bubbler) height was selected at each condition that maximized the multiplicand of efficiency and conversion ηX. This objective insured that reactor height H maximized energy use, but also converted substantial methane into hydrogen product:

$$H = \text{argmin}\,\eta X \qquad (35)$$

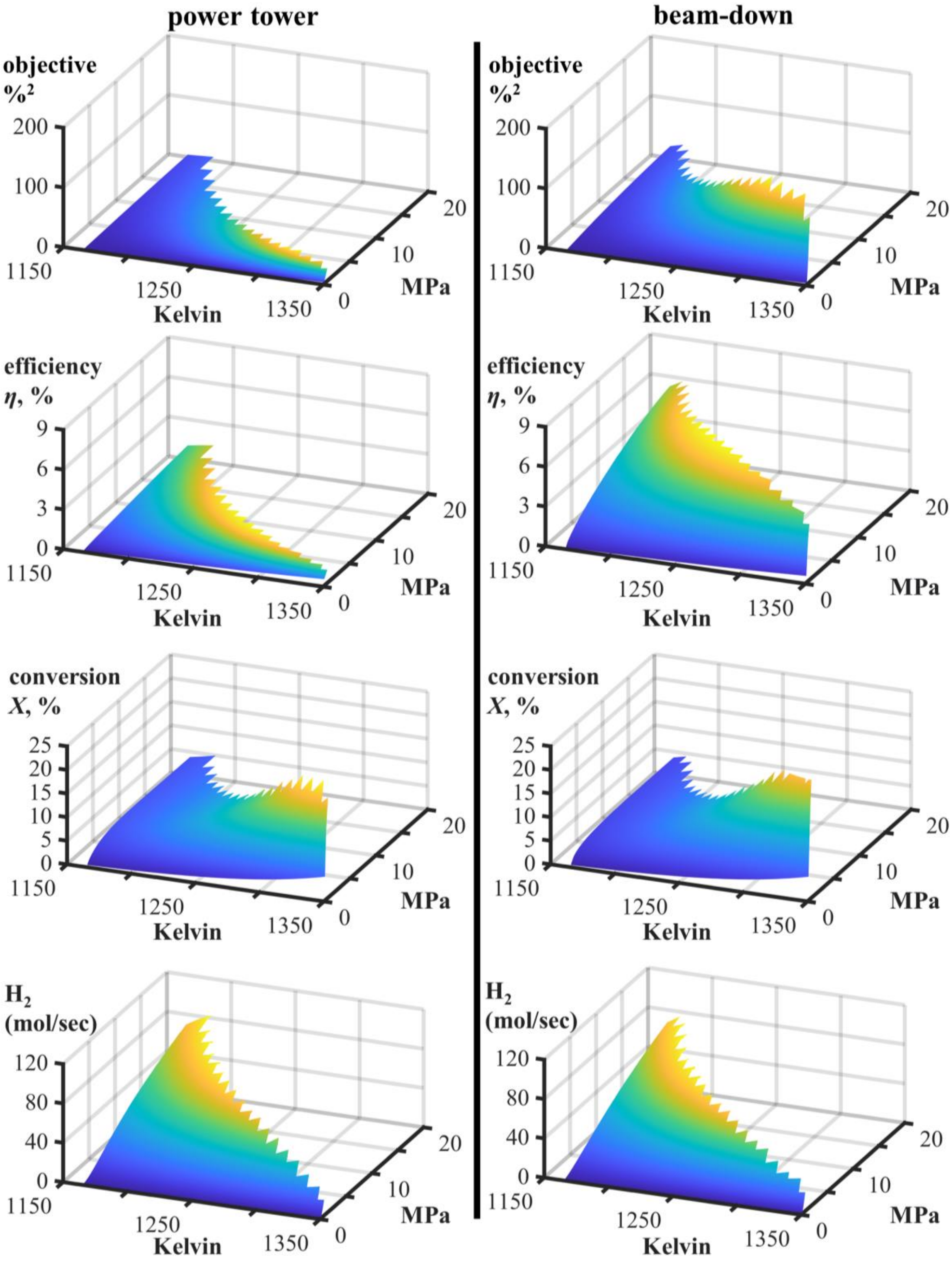

Figure 6. Performance metrics of alternative solar facilities for H_2 production.

As anticipated, efficiency was substantially higher in the beam-down reactor configuration. A maximum beam-down efficiency of 9% was discovered, whereas the most efficient power tower design was 1.7% efficient. Table 2 summarizes characteristics of the best designs on an objective or efficiency basis. Inefficiency of the power tower designs, which reemitted maximally 60 MW of radiation back to the environment, owed their exposed receivers. Conversely the cavity beam-down configuration, which approaches a blackbody as aspect ratio exceeds 4:1 [50,59–61], reemitted maximally 4.5 MW of radiation. These results are summarized in Figure 7. Convective power tower losses, modeled via validated semiempirical relations [43], were even higher. Power tower convection from the naked receiver approached 150 MW, while the nested beam-down receiver lost maximally 28 MW. This magnitude decrease in beam-down losses manifested as a magnitude increase in methane cracking efficiency. Relative to beam-down reactors, ineffective power tower energy use entailed large heliostat fields (Figure 8) despite the uniformity of other physical characteristics between the competing designs. Overall, results showed that power towers, despite their established use in electrical production, are unsuited to methane cracking for renewable hydrogen production.

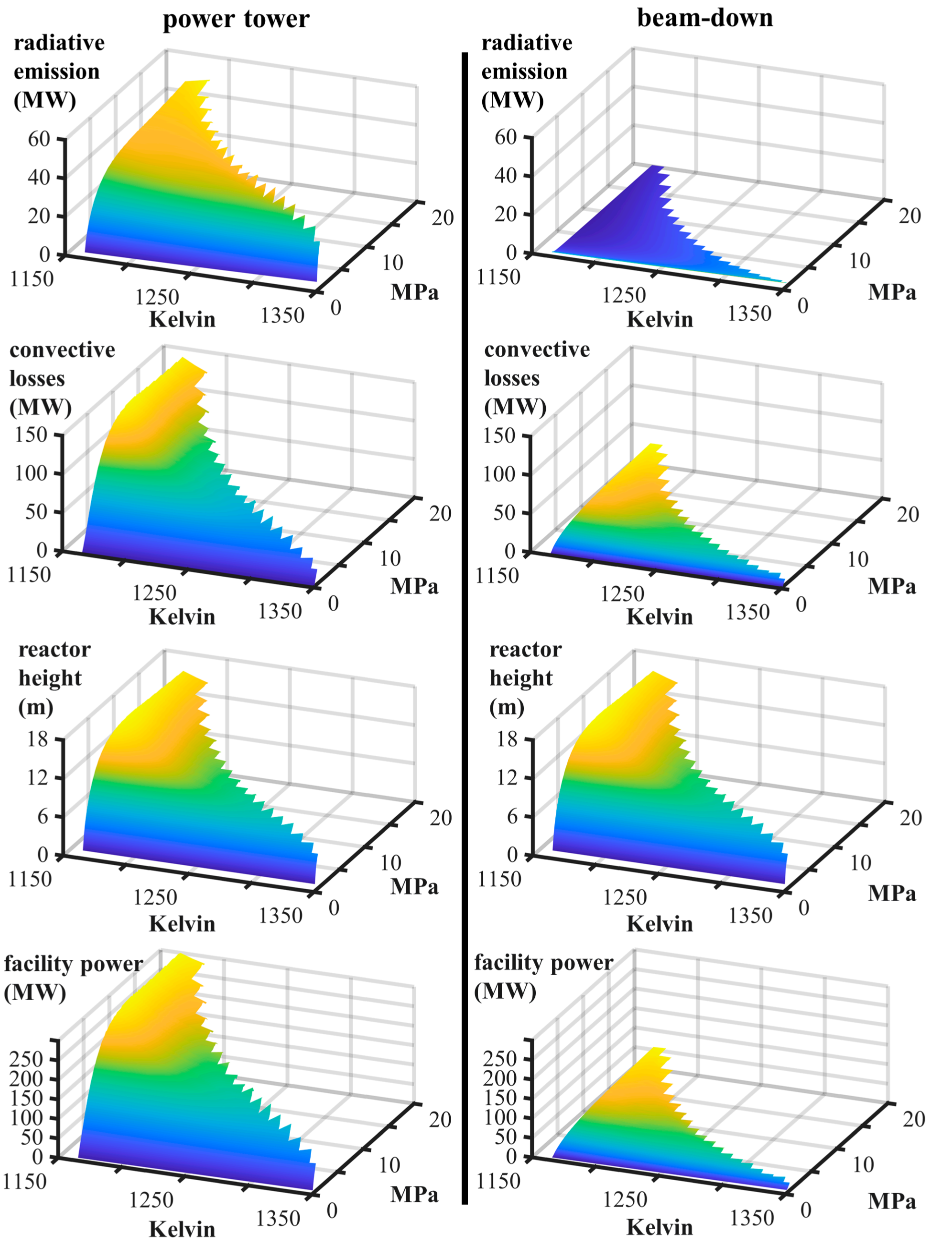

Figure 7. Losses and their contributing factors in alternative solar facilities for H_2 production.

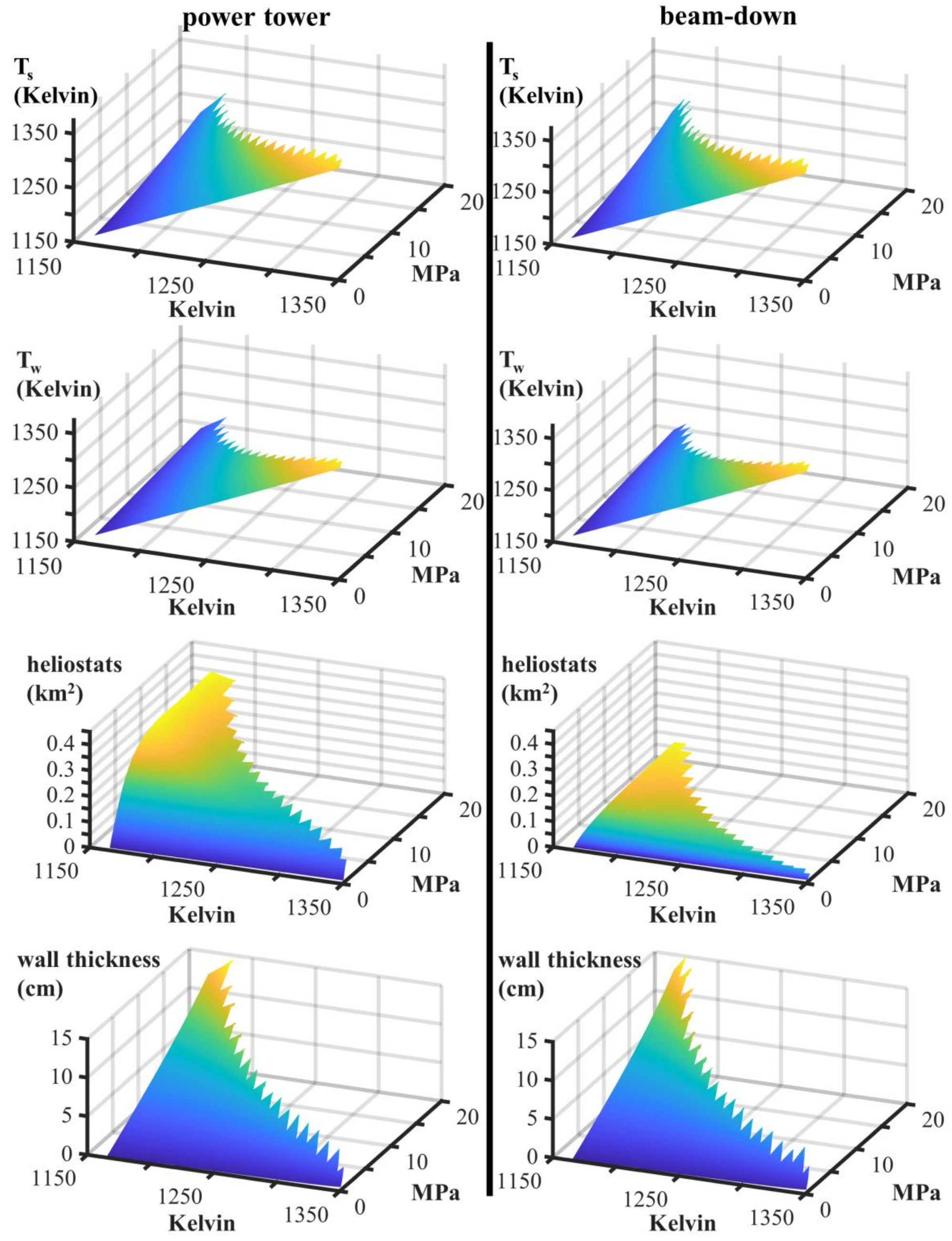

Figure 8. Characteristics of alternative solar facilities for H_2 production.

Table 2. The best simulated power tower and beam-down reactor designs across potential operating pressures from 2 to 200 atmospheres and 1150 to 1350 Kelvin.

		Power Tower		Beam-Down	
		Best Objective	**Best Efficiency**	**Best Objective**	**Best Efficiency**
objective, ηX	$\%^2$	33	22	152	102
efficiency, η	%	1.4	1.7	7.22	9
conversion X	%	23.6	12.9	21.1	11.3
isothermal reaction, T	Kelvin	1325	1265	1315	1255
inlet pressure, P_{inlet}	atm	21.71	65.13	24.67	69.10
facility power, Q_{field}	MW	144.3	190.0	24.7	34.1
convective losses, $Q_{convective}$	MW	39.6	72.5	10.5	15.22
radiative losses, $Q_{radiative}$	MW	38.1	42.4	1.4	1.00
H_2 produced	mol/sec	44.88	73.73	39.23	64.31

Table 2. *Cont.*

		Power Tower		Beam-Down	
		Best Objective	**Best Efficiency**	**Best Objective**	**Best Efficiency**
reactor height, H	meters	8.5	10.4	8.5	10.4
tube radius, $\mathfrak{R}$	meters	0.48	0.48	0.41	0.45
surface temperature, T_s	Kelvin	1365	1330	1348	1318
wall temperature, T_w	Kelvin	1350	1300	1337	1289
wall thickness, w	cm	6.10	8.40	3.85	7.47
heliostat area, $A_{mirrors}$	km^2	0.18	0.24	0.03	0.04

4. Discussion

Power tower designs showed poor energy efficiency in methane reaction for hydrogen production. This approach directed only 1.7% of incident solar radiation into fungible chemical fuel (H_2). Conversely, beam-down reactors achieved 9% efficiency. Although power tower and beam-down receivers were largely uniform in their reaction and physical characteristics (Figures 6–8), including ultimate reactant conversion to H_2 product, power towers showed radiative and convective energy losses a magnitude larger than beam-down designs (Figure 6). Overall power tower receivers, versus buried beam-down receivers, suffered from exposure and energy losses to the environment through convection and radiative emission. Poor power tower energy performance was highlighted by the large heliostat field a Solar Two tower would require (Figure 8). Figure 8 shows that although receiver temperatures and wall thicknesses were similar across facility operating conditions, the best power tower design demands a heliostat field of 0.18 km^2 to overcome radiative and convective losses. Conversely, the best beam-down heliostat field was 0.04 km^2, which likely entails lower facility capital and maintenance costs. Notably, 30–50% of solar facility costs are sunk in heliostat fields, which parasitically consume 3.8% of facility power and require persistent calibration [48,49,62–64].

All the simulated solar reactors showed low reactant methane conversion into hydrogen ($X < 30\%$, Figure 6). Conversion can be constrained by thermodynamics, kinetics, or heat transport [32]. To explore potential limitations Figure 9 plots the theoretical maximum conversion of methane at reactor effluent conditions against simulated conversion. Although Figure 9 shows regions where theoretical and simulated conversion converge or diverge, suggestive of thermodynamic or kinetic limitation, respectively, the best designs discovered were likely heat transport constrained. As shown in Table 2, heat movement drove large temperature gradients within the best discovered reactors. Although reaction occurred at 1255–1325 Kelvin, exterior receiver conditions were on the threshold of Inconel meltdown (1316–1365 Kelvin) under pressurized conditions (21.71–69.10 atm).

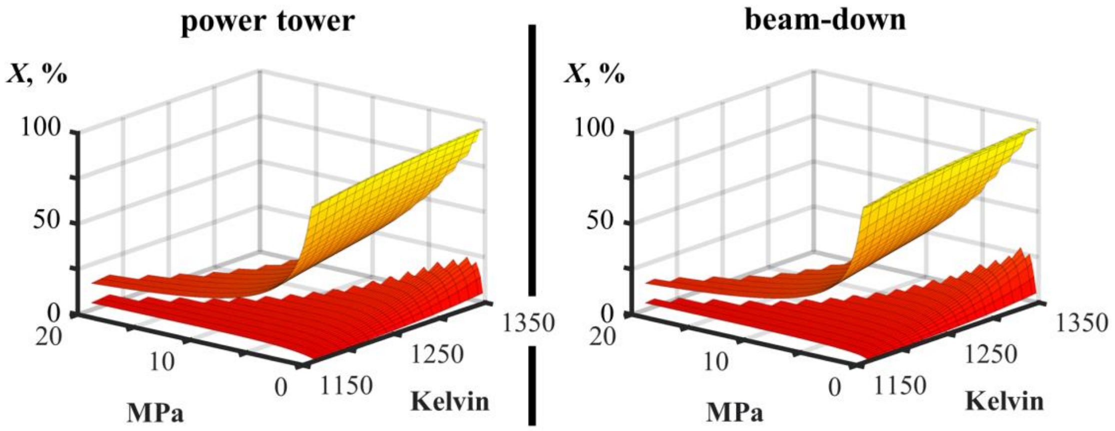

Figure 9. Approach to equilibrium in the power tower and beam-down reactor designs. The upper surface shows maximum theoretical conversion X at reactor effluent temperature and pressure. The lower surface shows actual conversion in the effluent of simulated reactors.

Higher external temperatures, which would drive added heat into reaction through larger conductive gradients, were constrained by Inconel's strength. Larger heat transfer area, which would open added paths for reaction heat, were constrained by receiver geometry. Thus, Solar Two commercial reactor concepts are likely thermally limited by Inconel physics and receiver geometry, not reaction thermodynamics or kinetics. Although power tower and beam-down receiver designs are mature in electrical generation [15], new solar designs are needed to fully realize the potential of methane cracking for hydrogen production. Ideally, a solar methane cracker is reaction-limited by thermodynamics or kinetics, not constrained by the ingress of solar heat. Under heat constraints, improvements in reaction catalysis may go unrealized. Recently, reaction catalysis with molten $MnCl_2$–KCl lowered the activation barrier for methane cracking to 160 kJ/mol [65], versus the 209 kJ/mol explored here. However, to fully leverage this breakthrough heat bottlenecks should be overcome with design innovation.

The new reactor model relied on assumptions common in chemical engineering practice, including well-mixed isothermal reaction and heat transfer via semiempirical Nusselt correlations (Appendix B) [18,31,32,43,44,66]. The Nusselt correlations were drawn from validated and published results [43,44,66]. Furthermore, presumably liquid metal catalysts bubble and vigorously mix to collapse thermal and material gradients. However, deeper multiphysics modeling and/or pilot plant experimentation is needed to test these assumptions. This work establishes solar methane cracking feasibility and facility conditions that can inform future rigorous multiphysics simulation and pilot plant operation. Future modeling, which appears worthwhile given results here that show hydrogen production efficiencies comparable to energy capture by photovoltaics [67], can explore the limitations of isothermal and Nusselt approximations.

5. Conclusions

Unlike prior work [3,19–22], here catalytic methane cracking explored expansive industrial conditions with a reversible kinetic model, a model that fit published data (Figures 3 and 4, Table 1). The model conformed to plug flow approximations used widely in chemical reactor design [18,31,32], yet still depended on catalytic surface [3]. Performance metrics and conditions were established for the future detailed multiphysics simulation of solar catalytic methane crackers. Contrary to previous analysis [68], a beam-down reactor, versus a power tower, was most feasible. The best discovered beam-down design was 9% efficient after radiative, convective, and heliostat losses. However, this mature commercial design was heat transfer limited, not reaction limited, which motivates research for new receiver configurations. Higher facility efficiencies are likely possible in solar reactors if heat debottlenecking realizes maximal reaction kinetics. Feasible solar hydrogen from established or new reactor concepts can be further converted to liquid ammonia for transportation use or burned directly in fuel cells [69]. Thus, clean solar catalytic molten hydrogen production is a promising transitional technology towards decarbonization [13]. Further studies that more deeply explore beam-down methane cracking physics, development, and heat transfer appear warranted.

Author Contributions: Conceptualization, A.W.W.; investigation, S.C.R.; supervision T.A.A. and J.T.E.S.; review and editing K.M.W. All authors have read and agreed to the published version of the manuscript.

Funding: This research received no external funding.

Conflicts of Interest: The authors declare no conflict of interest.

Appendix A

Appendix A.1 Greek Variable Definitions

α	fractional	effective absorptivity of a receiver surface from ray tracing
ε	fractional	effective emissivity of a receiver surface from ray tracing
η	%	energy efficiency of a solar receiver in hydrogen production
$\o$	meters	diameter of a vessel.
ρ	kg/m^3	density of molten 27% nickel, 73% bismuth [33,34]
ρ_{gas}	kg/m^4	gas density
ρ_{inlet}	kg/m^5	gas density at a reactor tube inlet temperature and pressure
σ	W/(m^{2}K^4)	Stefan–Boltzmann constant [$5.67\ldots \times 10^{-8}$ W/(m^{2}K^4)]
$\sigma_{YS}(T)$	Pa	Inconel temperature-dependent yield strength [46]

Appendix A.2 English Variable Definitions

A_{bubble}	m^2	area of bubble
$A_{bubblers}$	m^2	area of gas emanation on a gas distributor
A_{tube}	m^2	cross-sectional area of a bubbler (reactor) tube
b	bubbles	number of bubbles initiated by a gas distributor
$\dot{b}$	bubbles/sec	rate of bubble emanation from a gas distributor
$C_{p,i}$	J/(mol·Kelvin)	heat capacity of chemical species i
E_f	J/mol	forward reaction activation energy (Table 1)
E_r	J/mol	reverse reaction activation energy (Table 1)
F	fractional	view factor [16]
g	m/s^2	acceleration of gravity (9.81 m/s^2)
Gr	unitless	Grashoff number
h	W/(m^{2}Kelvin)	convective heat transfer coefficient to air [43]
h_{wall}	W/(m^{2}Kelvin)	convective heat transfer coefficient to molten metal [44]
H	meters	reactor tube manifold height
ΔH_{rxn}	J/mol	enthalpy of reaction
k_f	m/sec	forward Arrhenius preexponential (Table 1)
k_r	m^4/sec	reverse Arrhenius preexponential (Table 1)
$k(T)$	W/(m·Kelvin)	Inconel thermal conductivity at temperature T [46]
K_c	mol/m^3	concentration equilibrium constant
n	integer	number of tubes in a receiver manifold
$\dot{n}_{inlet}$	mol/sec	mole flow of reactor tube gaseous feed
n_C	moles	moles of solid carbon
n_{CH4}	moles	moles of gaseous methane
n_{H2}	moles	moles of gaseous hydrogen
$\dot{n}_C$	mol/sec	mole flow of solid carbon
$\dot{n}_{CH4}$	mol/sec	mole flow of gaseous methane
$\dot{n}_{H2}$	mol/sed	mole flow of gaseous hydrogen
Nu	unitless	Nusselt number
$N(r)$	W/m^2	flux at radial coordinate r in an Inconel tube wall
Pe	unitless	Peclet number
P_{inlet}	Pascals	reactor tube feed pressure
$P(z)$	Pascals	axial pressure in a reactor tube at elevation z
$Q_{convection}$	Watts	receiver losses to ambient air by natural convection
Q_{field}	Watts	solar energy incident on a heliostat field reflective area
$Q_{radiative}$	Watts	receiver emissive losses by radiation
Q_{wall}	Watts	energy that trespasses a reactor tube interior wall
$Q(z)$	m^3/sec	volumetric flow at elevation z in a reactor tube
r	meters	radial coordinate

r_{bubble}	meters	radius of a bubble
$r_{bubble,inlet}$	meters	initial radius of a bubble entering a reactor tube
R	J/(mol·Kelvin)	gas constant
$\mathfrak{R}$	meters	inner radius of a reactor tube
S	m^2	surface area of a solar receiver
t	seconds	time coordinate
T	Kelvin	isothermal reaction temperature
T_s	Kelvin	outer Inconel solar receiver surface temperature
T_w	Kelvin	inner Inconel reactor tube wall temperature
$v_{bubbler}$	m/sec	initial velocity of a bubble entering a reactor tube
V	m^3/sec	feed volumetric flow into a reactor tube
V_{bubble}	m^3	volume of a bubble
$V_{bubble,inlet}$	m^3	initial volume of a bubble entering a reactor tube
w	meters	reactor tube Inconel wall thickness
X	%	methane conversion to hydrogen gas
y_{CH4}	fractional	mole fraction of gaseous methane
y_{H2}	fractional	mole fraction of gaseous hydrogen
z	meters	axial coordinate (elevation in a reactor tube)
Z	unitless	compressibility factor from the SRK equation of state [35]

Appendix B

Physical Property Correlations

Density of molten 73% bismuth and 27% nickel liquid alloy (composition average) [33,34]:

$$\rho[\mathrm{kg/m^3}] = 0.27(\underbrace{9908 - 1.182T}_{liquid\ nickel\ \rho}) + 0.73(\underbrace{10665 - 1.1589T}_{liquid\ bismuth\ \rho}) \tag{A1}$$

Properties of Inconel solid [46]:

$$\sigma_{YS}[Pascals] = 733141411.067 - (2041707.776)T + (2286.861)T^2 - (0.861)T^3 \tag{A2}$$

$$\mathrm{k[W/(mK)]} = 6.7439 + (0.0166)T \tag{A3}$$

Determination of $\Delta H(T)$ from the van t′ Hoff equation for regression initialization [13,32,70]:

$$\Delta H(T) = \Delta H^o(T) + \int_T^{298} C_{p,CH_4}(T)dT + \int_{298}^{T} [C_{p,C}(T) + 2C_{p,H_2}(T)]dT \tag{A4}$$

$$\Delta H^o(T) = 75\ \mathrm{kJ/mol} \tag{A5}$$

$$C_{p,species}[\mathrm{J/(mol{\cdot}Kelvin)}] = a_1 + a_2T + a_3T^2 + a_4T^3 \tag{A6}$$

Table A1. Coefficients for use in Equation (A6).

Species	a_1	a_2	a_3	a_4
CH_4	18.386286	$5.470402(10^{-2})$	$1.034479(10^{-5})$	$-9.833387(10^{-9})$
C	−5.394667	$5.812952(10^{-2})$	$-4.177213(10^{-5})$	$-1.071678(10^{-8})$
H_2	28.653517	$7.762754(10^{-4})$	$1.324842(10^{-7})$	$6.664873(10^{-10})$

Power tower convective heat transfer coefficient to the ambient air [43]:

$$Nu = 0.052(Gr)^{0.36} \tag{A7}$$

Beam-down cavity convective heat transfer coefficient to the ambient air [43]:

$$Nu = 0.088(Gr)^{1/3}(T_s/298)^{0.18} \tag{A8}$$

Molten metal convective heat transfer coefficient [44]:

$$Nu = 4.8 + 0.025Pe^{0.8} \tag{A9}$$

Effective emissivity of the corrugated power tower receiver surface from 2D ray tracing for a material emissivity of 0.95 [50]:

$$\varepsilon = 0.644 + (0.066)\mathfrak{R}, \quad \mathfrak{R} \in [0.01 - 0.50 \text{ meters}] \tag{A10}$$

where all radiative emission and reflection was assumed diffuse. Note that although the material emissivity was 0.95, light traps in receiver manifold corrugations to suppress reradiation escape.

Effective absorptivity of the corrugated power tower receiver surface from 2D ray tracing for a material absorptivity of 0.95 [50]:

$$\alpha = 0.959 - (0.002)\mathfrak{R}, \quad \mathfrak{R} \in [0.01 - 0.50 \text{ meters}] \tag{A11}$$

where all radiative reflection was assumed diffuse. Note that although the material absorptivity was 0.95, light traps in receiver manifold corrugations to inflate absorptivity.

Effective emissivity of the corrugated beam-down receiver surface from 2D ray tracing for a material emissivity of 0.95 [50]:

$$\varepsilon = 0.642 - (0.084)\mathfrak{R}, \quad \mathfrak{R} \in [0.01 - 0.50 \text{ meters}] \tag{A12}$$

where all radiative emission and reflection was assumed diffuse. Note that although the material emissivity was 0.95, light traps in receiver manifold corrugations to suppress reradiation escape.

Effective absorptivity of the corrugated beam-down receiver from 2D ray tracing for a material absorptivity of 0.95 [50]:

$$\alpha = 0.959 + (0.003)\mathfrak{R}, \quad \mathfrak{R} \in [0.01 - 0.50 \text{ meters}] \tag{A13}$$

where all radiative reflection was assumed diffuse. Note that although the material absorptivity was 0.95, light traps in receiver manifold corrugations to inflate absorptivity.

View factor for power tower diffuse emission to the environment:

$$F = 1 \tag{A14}$$

View factor for beam-down cavity tube manifold diffuse emission and diffuse reflection to the environment [16]:

$$F = 1 - \frac{1}{2}\sqrt{\left(2 + \left(\frac{H}{2.55}\right)^2\right)^2 - 4} - \frac{1}{2}\left(\frac{H}{2.55}\right)^2 \tag{A15}$$

Specifically, Equation (A15) corresponds to the Howell Catalog of Radiation View Factors entry C−80 for a disc and cylinder radius of 2.55 m, which corresponds to the Solar Two manifold diameter of 5.1 m [14].

View factor for beam-down cavity cylinder base (bottom) diffuse emission and diffuse reflection to the environment [16].

$$F = \frac{1}{2}\left(\left(\frac{H}{2.55}\right)^2\left(2\left(\frac{2.55}{H}\right)^2+1\right) - \sqrt{\left(\left(\frac{H}{2.55}\right)^2\left(2\left(\frac{2.55}{H}\right)^2+1\right)\right)^2 - 4}\right) \quad \text{(A16)}$$

Specifically, Equation (A16) corresponds to the Howell Catalog of Radiation View Factors C-40 for discs of radius of 2.55 m, which corresponds to the Solar Two manifold diameter of 5.1 m [14].

References

1. Loutzenhiser, P.G.; Muroyama, A.P. A review of the state-of-the-art in solar-driven gasification processes with carbonaceous materials. *Sol. Energy* **2017**, *156*, 93–100. [CrossRef]
2. Palmer, C.; Upham, D.C.; Smart, S.; Gordon, M.J.; Metiu, H.; McFarland, E.W. Dry reforming of methane catalysed by molten metal alloys. *Nat. Catal.* **2020**, *3*, 83–89. [CrossRef]
3. Upham, D.C.; Agarwal, V.; Khechfe, A.; Snodgrass, Z.R.; Gordon, M.J.; Metiu, H.; McFarland, E.W. Catalytic molten metals for the direct conversion of methane to hydrogen and separable carbon. *Science* **2017**, *358*, 917–921. [CrossRef] [PubMed]
4. Henry, A.; Prasher, R.; Majumdar, A. Five thermal energy grand challenges for decarbonization. *Nat. Energy* **2020**, *5*, 635–637. [CrossRef]
5. Ehrhart, B.D.; Muhich, C.L.; Al-Shankiti, I.; Weimer, A.W. System efficiency for two-step metal oxide solar thermochemical hydrogen production—Part 3: Various methods for achieving low oxygen partial pressures in the reduction reaction. *Int. J. Hydrogen Energy* **2016**, *41*, 19904–19914. [CrossRef]
6. Ehrhart, B.D.; Muhich, C.L.; Al-Shankiti, I.; Weimer, A.W. System efficiency for two-step metal oxide solar thermochemical hydrogen production—Part 1: Thermodynamic model and impact of oxidation kinetics. *Int. J. Hydrogen Energy* **2016**, *41*, 19881–19893. [CrossRef]
7. Ehrhart, B.D.; Muhich, C.L.; Al-Shankiti, I.; Weimer, A.W. System efficiency for two-step metal oxide solar thermochemical hydrogen production—Part 2: Impact of gas heat recuperation and separation temperatures. *Int. J. Hydrogen Energy* **2016**, *41*, 19894–19903. [CrossRef]
8. Scheffe, J.R.; Steinfeld, A. Oxygen exchange materials for solar thermochemical splitting of H_2O and CO_2: A review. *Mater. Today* **2014**, *17*, 341–348. [CrossRef]
9. Carrillo, R.J.; Scheffe, J.R. Advances and trends in redox materials for solar thermochemical fuel production. *Sol. Energy* **2017**, *156*, 3–20. [CrossRef]
10. Bader, R.; Lipiński, W. Solar thermochemical processes. In *Solar Energy*; World Scientific: Hackensack, NJ, USA, 2016; pp. 345–394.
11. Binotti, M.; Di Marcoberardino, G.; Biassoni, M.; Manzolini, G. Solar hydrogen production with cerium oxides thermochemical cycle. In *Proceedings of the AIP Conference Proceedings*; AIP Publishing LLC: Melville NY, USA, 2017; Volume 1850, p. 100002.
12. Giostri, A.; Binotti, M.; Sterpos, C.; Lozza, G. Small scale solar tower coupled with micro gas turbine. *Renew. Energy* **2020**, *147*, 570–583. [CrossRef]
13. Weger, L.; Abánades, A.; Butler, T. Methane cracking as a bridge technology to the hydrogen economy. *Int. J. Hydrogen Energy* **2017**, *42*, 720–731. [CrossRef]
14. Pacheco, J.E.; Bradshaw, R.W.; Dawson, D.B.; De la Rosa, W.; Rockwell, G.; Goods, H.S.; Hale, M.J.; Jacobs, P. *Final Tests and Evaluation Results from the Solar Two Project*; Sandia National Labs: Albuqerque, NM, USA, 2002; pp. 1–21.
15. Ho, C.K.; Iverson, B.D. Review of high-temperature central receiver designs for concentrating solar power. *Renew. Sustain. Energy Rev.* **2014**, *29*, 835–846. [CrossRef]
16. Howell, J.R.; Menguc, M.P.; Siegel, R. *Thermal Radiation Heat Transfer*; CRC Press: Boca Raton, FL, USA, 2010; ISBN 1-4398-9455-8.
17. Diago, M.; Calvet, N.; Armstrong, P.R. Net power maximization from a faceted beam-down solar concentrator. *Sol. Energy* **2020**, *204*, 476–488. [CrossRef]

18. Turton, R.; Bailie, R.C.; Whiting, W.B.; Shaeiwitz, J.A. *Analysis, Synthesis and Design of Chemical Processes*; Pearson Education: London UK, 2008; ISBN 0-13-245918-3.
19. Parkinson, B.; Tabatabaei, M.; Upham, D.C.; Ballinger, B.J.; Greig, C.; Smart, S.; McFarland, E. Hydrogen production using methane: Techno-economics of decarbonizing fuels and chemicals. *Int. J. Hydrogen Energy* **2018**, *43*, 2540–2555. [CrossRef]
20. Trommer, D.; Hirsch, D.; Steinfeld, A. Kinetic investigation of the thermal decomposition of CH4 by direct irradiation of a vortex-flow laden with carbon particles. *Int. J. Hydrogen Energy* **2004**, *29*, 627–633. [CrossRef]
21. Paxman, D.; Trottier, S.; Flynn, M.R.; Kostiuk, L.; Secanell, M. Experimental and numerical analysis of a methane thermal decomposition reactor. *Int. J. Hydrogen Energy* **2017**, *42*, 25166–25184. [CrossRef]
22. Steinberg, M. Production of hydrogen and methanol from natural gas with reduced CO_2 emission. *Int. J. Hydrogen Energy* **1998**, *23*, 419–425. [CrossRef]
23. Blackwood, J.D. The kinetics of the system carbon-hydrogen-methane. *Aust. J. Chem.* **1962**, *15*, 397–408. [CrossRef]
24. Blackwood, J.D. The reaction of Carbon with Hydrogen at High Pressure. *Aust. J. Chem.* **1959**, *12*, 14–28. [CrossRef]
25. Gulbransen, E.A.; Andrew, K.F.; Brassart, F.A. The reaction of hydrogen with graphite at 1200° to 1650 °C. *J. Electrochem. Soc.* **1965**, *112*, 49–52. [CrossRef]
26. Hedden, K. The formation of methane from hydrogen and carbon at high temperatures and pressures. *Z. Elektrochem. Angew. Phys. Chem.* **1962**, *60*, 125–131.
27. Parolin, G.; Borgognga, A.; Iaquaniello, G.; Salladini, A.; Cerbelli, S. Deactivation-induced dynamics of the reaction front in a fixed-bed catalytic membrane reactor: Methane cracking as a case study. *Int. J. Hydrogen Energy* **2020**. [CrossRef]
28. Pring, J.N.; Fairlie, D.M. X.—The methane equilibrium. *J. Chem. Soc. Trans.* **1912**, *101*, 91–103. [CrossRef]
29. Catalan, L.J.; Rezaei, E. Coupled hydrodynamic and kinetic model of liquid metal bubble reactor for hydrogen production by noncatalytic thermal decomposition of methane. *Int. J. Hydrogen Energy* **2020**, *45*, 2486–2503. [CrossRef]
30. Keipi, T.; Li, T.; Løvås, T.; Tolvanen, H.; Konttinen, J. Methane thermal decomposition in regenerative heat exchanger reactor: Experimental and modeling study. *Energy* **2017**, *135*, 823–832. [CrossRef]
31. Luyben, W.L. *Principles and Case Studies of Simultaneous Design*; Wiley: Hoboken, NJ, USA, 2011; ISBN 978-0-470-92708-3.
32. Rawlings, J.B.; Ekerdt, J.G. *Chemical Reactor Analysis and Design Fundamentals*; Nob Hill Pub, LLC.: Madison WS, USA, 2002; ISBN 0-615-11884-4.
33. Cahill, J.A.; Kirshenbaum, A.D. The density of liquid bismuth from its melting point to its normal boiling point and an estimate of its critical constants. *J. Inorg. Nucl. Chem.* **1963**, *25*, 501–506. [CrossRef]
34. Grosse, A.V.; Kirshenbaum, A. The densities of liquid iron and nickel and an estimate of their critical temperature. *J. Inorg. Nucl. Chem.* **1963**, *25*, 331–334. [CrossRef]
35. Soave, G. Equilibrium constants from a modified Redlich-Kwong equation of state. *Chem. Eng. Sci.* **1972**, *27*, 1197–1203. [CrossRef]
36. Seader, J.D.; Henley, E.J.; Roper, D.K. *Separation Process Principles*; Wiley: New York, NY, USA, 1998; Volume 25.
37. Eldridge, R.B.; Fair, J.R. Sieve-tray extractor continuous-phase mixing. *Ind. Eng. Chem. Res.* **1999**, *38*, 218–222. [CrossRef]
38. Eldridge, R.B.; Humphrey, J.L.; Fair, J.R. Continuous Phase Mixing on Crossflow Extraction Sieve Trays. *Sep. Sci. Technol.* **1987**, *22*, 1121–1134. [CrossRef]
39. Davies, R.M.; Taylor, G.I. The mechanics of large bubbles rising through extended liquids and through liquids in tubes. *Proc. R. Soc. Lond. Ser. A Math. Phys. Sci.* **1950**, *200*, 375–390.
40. Bohn, M.S. Experimental investigation of the direct absorption receiver concept. *Energy* **1987**, *12*, 227–233. [CrossRef]
41. Martinek, J.; Weimer, A.W. Design considerations for a multiple tube solar reactor. *Sol. Energy* **2013**, *90*, 68–83. [CrossRef]
42. Klingensmith, L. Development of Extruded Heavy-Wall Large Diameter Nickel-Base Alloy Piping for AUSC Power Plants. In Proceedings of the Asian Coalition for Climate and Energy, Shanghai, China, 23–26 August 2011; pp. 272–298.
43. Boehm, R.F. A Review of Convective Loss Data from Solar Central Receivers. *J. Sol. Energy Eng.* **1987**, *109*, 101–107. [CrossRef]

44. *Metals, U.S.O. of N.R.C. on the B.P. of L. Liquid-Metals Handbook*; US Government Printing Office: Washington DC, USA, 1954; Volume 2.
45. Bird, R.B.; Stewart, W.E.; Lightfoot, E.N.; Meredith, R.E. Transport phenomena. *J. Electrochem. Soc.* **1961**, *108*, 78C. [CrossRef]
46. *Incoloy Alloy 800H & 800HT*; Special Metals Corporation: Huntington, WV, USA, 2004.
47. Behar, O.; Khellaf, A.; Mohammedi, K. A review of studies on central receiver solar thermal power plants. *Renew. Sustain. Energy Rev.* **2013**, *23*, 12–39. [CrossRef]
48. Bhargav, K.R.; Gross, F.; Schramek, P. Life Cycle Cost Optimized Heliostat Size for Power Towers. *Energy Procedia* **2014**, *49*, 40–49. [CrossRef]
49. Mancini, T.R.; Gary, J.A.; Kolb, G.J.; Ho, C.K. *Power Tower Technology Roadmap and Cost Reduction Plan*; SAND2011-2419; Sandia National Laboratories: Albuquerque, NM, USA, 2011; p. 7.
50. Rowe, S.C.; Groehn, A.J.; Palumbo, A.W.; Chubukov, B.A.; Clough, D.E.; Weimer, A.W.; Hischier, I. Worst-case losses from a cylindrical calorimeter for solar simulator calibration. *Opt. Express* **2015**, *23*, A1309–A1323. [CrossRef]
51. Rowe, S.C.; Hischier, I.; Palumbo, A.W.; Chubukov, B.A.; Wallace, M.A.; Viger, R.; Lewandowski, A.; Clough, D.E.; Weimer, A.W. Nowcasting, predictive control, and feedback control for temperature regulation in a novel hybrid solar-electric reactor for continuous solar-thermal chemical processing. *Sol. Energy* **2018**, *174*, 474–488. [CrossRef]
52. Skinrood, A.C.; Brumleve, T.D.; Schafer, C.T.; Yokomizo, C.T.; Leonard, C.M., Jr. *Status Report on a High Temperature Solar Energy System*; Sandia National Lab. (Albuquerque-NM): Albuquerque, NM, USA, 1974.
53. Slocum, A.H.; Codd, D.S.; Buongiorno, J.; Forsberg, C.W.; McKrell, T.J.; Nave, J.-C.; Papanicolas, C.N.; Ghobeity, A.; Noone, C.J.; Passerini, S.; et al. Concentrated solar power on demand. *Sol. Energy* **2011**, *85*, 1519–1529. [CrossRef]
54. Smith, J.M. *Introduction to Chemical Engineering Thermodynamics*; ACS Publications: Washington, DC, USA, 2004; ISBN 0073104450.
55. Yu, X. Thermodynamics and Kinetics of Gasification Reactions of Metallurgical Cokes. Ph.D. Thesis, University of London, London, UK, 1988.
56. De Bokx, P.K.; Kock, A.H.; Boellaard, E.; Klop, W.; Geus, J.W. The formation of filamentous carbon on iron and nickel catalysts: I. Thermodynamics. *J. Catal.* **1985**, *96*, 454–467. [CrossRef]
57. Levenspiel, O. Chemical reaction engineering. *Ind. Eng. Chem. Res.* **1999**, *38*, 4140–4143. [CrossRef]
58. Wetzel, T.; Pacio, J.; Marocco, L.; Weisenburger, A.; Heinzel, A.; Hering, W.; Schroer, C.; Muller, G.; Konys, J.; Stieglitz, R.; et al. Liquid metal technology for concentrated solar power systems: Contributions by the German research program. *AIMS Energy* **2014**, *2*, 89–98. [CrossRef]
59. Sefkow, E.A.B. The Design of a Calorimeter to Measure Concentrated Solar Flux. Master's Thesis, The University of Minnesota, Minnesota, MN, USA, 2013.
60. Sparrow, E.M. *Radiation Heat Transfer*; Routledge and CRC Press: Boca Raton, FL, USA, 2018; ISBN 1-351-42010-0.
61. Sarwar, J.; Georgakis, G.; Kouloulias, K.; Kakosimos, K.E. Experimental and numerical investigation of the aperture size effect on the efficient solar energy harvesting for solar thermochemical applications. *Energy Convers. Manag.* **2015**, *92*, 331–341. [CrossRef]
62. Berenguel, M.; Rubio, F.R.; Valverde, A.; Lara, P.J.; Arahal, M.R.; Camacho, E.F.; López, M. An artificial vision-based control system for automatic heliostat positioning offset correction in a central receiver solar power plant. *Sol. Energy* **2004**, *76*, 563–575. [CrossRef]
63. Relloso, S.; García, E.A. Tower Technology Cost Reduction Approach after Gemasolar Experience. *Energy Procedia* **2015**, *69*, 1660–1666. [CrossRef]
64. Binotti, M.; De Giorgi, P.; Sánchez, D.; Manzolini, G. Comparison of Different Strategies for Heliostats Aiming Point in Cavity and External Tower Receivers. *J. Sol. Energy Eng.* **2016**, *138*, 021008. [CrossRef]
65. Kang, D.; Rahimi, N.; Gordon, M.J.; Metiu, H.; McFarland, E.W. Catalytic methane pyrolysis in molten MnCl2-KCl. *Appl. Catal. B Environ.* **2019**, *254*, 659–666. [CrossRef]
66. Kuipers, J.A.M.; Van Swaaij, W.P.M. Application of computational fluid dynamics to chemical reaction engineering. *Rev. Chem. Eng.* **1997**, *13*, 1–118. [CrossRef]
67. Roeb, M.; Neises, M.; Monnerie, N.; Sattler, C.; Pitz-Paal, R. Technologies and trends in solar power and fuels. *Energy Environ. Sci.* **2011**, *4*, 2503–2511. [CrossRef]
68. Vant-Hull, L. Issues with Beam-down Concepts. *Energy Procedia* **2014**, *49*, 257–264. [CrossRef]

69. Christensen, C.H.; Johannessen, T.; Sørensen, R.Z.; Nørskov, J.K. Towards an ammonia-mediated hydrogen economy? *Catal. Today* **2006**, *111*, 140–144. [CrossRef]
70. Linstrom, P.J.; Mallard, W.G. The NIST Chemistry WebBook: A Chemical Data Resource on the Internet. *J. Chem. Eng. Data* **2001**, *46*, 1059–1063. [CrossRef]